Progress in Additive Manufacturing
https://doi.org/10.1007/s40964-022-00334-2

FULL RESEARCH ARTICLE

A novel heat treatment of the additively manufactured Co28Cr6Mo biomedical alloy and its effects on hardness, microstructure and sliding wear behavior

Lavinia Tonelli[1] · **Mohamed M. Z. Ahmed**[2,3] · **Lorella Ceschini**[1]

Received: 25 October 2021 / Accepted: 30 July 2022

Abstract
Co28Cr6Mo alloy (ASTM F75 and F1537) is one of the standard biomaterials for permanent orthopedic implants, utilized especially in case of joint replacement, such as knee and ankle prostheses. At the present, innovative Additive Manufacturing (AM) technologies, such as laser-based powder bed fusion (LPBF), also known as selective laser melting (SLM), enable the production of customized medical devices with improved mechanical properties. When dealing with implants for joint replacement, wear resistance is critical and, unlike compressive and tensile properties, the knowledge on wear behavior of the LPBF Co28Cr6Mo alloy is currently limited. Furthermore, the effect of post-process heat treatment on tribological properties, that have to be customized on the peculiar microstructure induced by LPBF, needs to be assessed. In this view, the present work first focuses on a novel direct aging treatment of the LPBF Co28Cr6Mo alloy, performed in the range 600–900 °C up to 180 min, and investigates the effects on hardness and microstructural features, with the optimized heat-treated condition found in case of 850 °C for 180 min aging treatment. Then, the attention is driven to the dry sliding wear behavior of as-built and heat-treated LPBF Co28Cr6Mo alloy, considering the conventional wrought alloy as benchmark. For testing conditions closer to the in-service ones, the as-built LPBF alloy showed a wear resistance higher than the conventional wrought alloy. The optimized aging treatment significantly modified the as-built LPBF microstructure, it improved the alloy hardness and, in general, it positively affected its friction and wear behavior.

Keywords Powder bed fusion (PBF) · Selective laser melting (SLM) · Additive manufacturing (AM) · Biomaterial · Co alloys · Microstructure · Heat treatment · Wear

1 Introduction

Cobalt–chromium–molybdenum (CoCrMo) alloys benefit from good mechanical properties, high wear and corrosion resistance, and high biocompatibility, that make them suitable for biomedical applications [1]. These alloys, in particular the Co28Cr6Mo one, are usually adopted for the manufacturing of permanent implants for joint replacement (i.e., hip, knee, and ankle prostheses) by forging or casting. Recently, the opportunity of applying innovative additive manufacturing technologies, such as the laser powder bed fusion (LPBF) one, to these alloys has been studied in the literature [2–5]. The main upside of using this technology in the biomedical field lies in the possibility of tailoring the prostheses design on the patient actual needs. LPBF is based on the selective melting of subsequent layers of fine metallic powders and literature shows that, if the LPBF process is properly optimized, Co28Cr6Mo parts are characterized by a near-full density and a high mechanical strength [2, 5–7]. The mechanical strength, higher than conventional forged or cast parts, is mainly ascribable to the extremely fine, metastable and supersaturated microstructure achievable in the as-built LPBF parts [8], inducing grain refinement and solid solution strengthening. Further strengthening can

✉ Lavinia Tonelli
lavinia.tonelli2@unibo.it

[1] Department of Industrial Engineering (DIN), Alma Mater Studiorum - University of Bologna, Viale del Risorgimento 4, 40136 Bologna, Italy

[2] Mechanical Engineering Department, College of Engineering et al Kharj, Prince Sattam Bin Abdulaziz University, Al Kharj 16273, Saudi Arabia

[3] Department of Metallurgical and Materials Engineering, Faculty of Petroleum and Mining Engineering, Suez University, Suez 43512, Egypt

Published online: 24 August 2022

be obtained by a dedicated heat treatment aimed, for this specific alloy, at promoting the transformation in the high-strength Co hexagonal close-packed (hcp) lattice structure together with fine carbide precipitation. In this view, the conventional alloy is generally subjected to an aging anneal preceded by high temperature forging in case of wrought alloys, or by a high temperature solution treatment and quenching in case of cast alloys [9]. However, the heat treatment of the LPBF alloy has to be re-designed on the basis of its peculiar fine, metastable and supersaturated microstructure. Such microstructure is, in fact, able to promote the precipitation of second phases during an aging treatment performed directly from the as-built condition, thus avoiding high temperature treatments that induce grain coarsening and, therefore, reduce or suppress the strengthening due to grain refinement. The effectiveness of the direct aging of LPBF alloys has been already verified in the literature for other metallic materials, such as aluminum alloys [10–12]. However, in the case of the Co28Cr6Mo LPBF alloy a quite limited work has been carried out on direct aging, since so far, researches mainly focused on long-time annealing [4, 13] or solution treatment with and without a subsequent aging [14–17]. Furthermore, literature up to now has predominantly investigated static mechanical properties (hardness and tensile behavior) of the Co28Cr6Mo LPBF alloy, both in the as-built and heat-treated state, while there is a substantially lack of data concerning its wear behavior. As this alloy is used to fabricate joint replacement prostheses, its wear resistance is of primary importance.

In fact, metallic materials for joint replacement must assure a high wear resistance, since failure of the implant is often due to wear-related issues that induce the formation of wear debris possibly leading to inflammatory reactions [18]. Modern prostheses are of the metal-on-polymer type, in which a polymeric insert (usually made of ultra-high molecular weight polyethylene, UHMWPE) is interposed between the two metallic surfaces replacing the joint [19]. In these devices, the polymeric insert undergoes wear phenomena; however, wear of the metal alloy can still occur in correspondence of metal-on-metal modular junctions, where micro-motions between the two components might be developed [20]. It should also be considered that the wear debris of the polyethylene used for the insert cause particle-induced osteolysis that often leads to implant failure and revision surgery [21], especially in case of knee prostheses, where the complex geometries of the bearing surfaces lead to multiple motion conditions [22, 23]. Furthermore, the lifespan of metals-on-polymer prostheses lies in the range 15–25 years; therefore, their application to young people is limited [24]. As an alternative, a metal-on-metal configuration can be adopted. In this configuration, the best option is to fabricate both surfaces in the CoCrMo alloys, that assure a good trade-off between wear and corrosion resistance [19]. In fact, in this type of prostheses wear rate is very low, much lower than for metal-on-polymer ones, assuring a longer lifespan [24]. However, the adverse reactions induced by metallic wear debris have raised major concerns in the science community [25–27]. Therefore, it is evident that the assessment of the wear resistance of CoCrMo alloys is critical and, to the best of the authors knowledge, lack of data assessing tribological behavior of LPBF processed Co28Cr6Mo alloy currently exists, both in the as-built condition and after heat treatment.

Based on the above, the present study aims to define the heat treatment conditions capable to optimize hardness of the LPBF Co28Cr6Mo alloy and to carry out a preliminary characterization of its wear behavior. In view of the extremely fine, supersaturated and metastable microstructure resulting from LPBF, in the present work only short-time (30–180 min) aging treatments in the range 600–900 °C, without a preliminary solution treatment, were considered. The effects on alloy hardness and microstructure were first investigated to identify the optimized aging conditions. Once identified, tribological tests were conducted on both aged and as-built samples and results were compared to the conventional wrought alloy.

2 Experimental

Samples were produced using an LPBF machine (SISMA MYSINT100), equipped with a 200 W fiber laser and a 55 µm spot diameter. Parallelepiped samples ($6 \times 20 \times 30$ mm^3) were built in a nitrogen atmosphere (oxygen < 0.3 vol.%) at ambient temperature, starting from Co28Cr6Mo spherical powders supplied by LPW Technology (currently LPW Carpenter Additive, Carpenter Technology Corporation, USA). A chessboard scanning strategy and a vertical building direction (perpendicular to the building platform) were adopted.

The chemical composition provided by the supplier is reported in Table 1 and fulfils the specifications of ASTM F75 and ASTM F1537 [28, 29] standards for surgical permanent implants made of Co28Cr6Mo alloy.

According to previous investigations [30–32], Laser Energy Density (LED) has proved to be a reliable parameter to define the overall quality of the LPBF Co28Cr6Mo alloy, especially in terms of defects content. Therefore, aging treatment assessment was carried out on samples produced with LED able to induce near-full density. Six LED values were considered, ranging between 120 and 180 Jmm^{-3}; these LED values were obtained considering different process parameters combinations, summarized in Table 2.

Samples for heat treatment assessment were used to verify the repeatability of aging treatment and to identify the optimized conditions in terms of maximum alloy hardness.

Table 1 Chemical composition (wt.%) of Co28Cr6Mo feedstock powder used for the production of LPBF samples, provided by LPW Technology

Elements (wt.%)										
Co	Cr	Mo	Si	Mn	Fe	Ni	C	W	Ti	O
Bal	27.00–30.00	5.00–7.00	< 1.00	< 1.00	< 0.75	0.25–0.50	< 0.16	< 0.20	< 0.10	< 0.10

Table 2 Process parameters adopted for the fabrication of Co28Cr6Mo LPBF samples for heat treatment assessment

Laser Power [W]	Scanning velocity [mm s^{-1}]	Hatch spacing [mm]	Layer thickness [mm]	LED [J mm^{-3}]
90; 130; 150	900; 500	0.04; 0.06	0.02; 0.03	120–180

Then, tribological tests were carried out on a different set of samples, whose details are disclosed in Table 3. As no reference data on the wear behavior of the Co28Cr6Mo alloy is currently reported in the literature, tribological tests were carried out both on samples obtained in the optimized LED range and on samples obtained outside this range. In this way, also the effect of surface defects, due to un-optimized process parameters, on the wear behavior is taken into consideration. Therefore, samples were fabricated with low (L and L-HT), medium (M and M-HT), and high (H, H-HT) LED values, leading to different density values (Table 3). The acronym HT identifies samples heat-treated in the optimized aging condition (850 °C for 180 min), as will be discussed in the following.

2.1 Heat treatment assessment

Direct aging treatments were carried out on the as-built samples in a muffle furnace operating at ambient atmosphere and were followed by air cooling. Aging temperatures were chosen in the range 600–900 °C (600, 700, 750, 800, 850, 900 °C were tested) on the basis of the time–temperature–precipitation (TTP) curves published by Taylor and Waterhouse [33] with the aim of inducing alloy aging and the isothermal phase transformation from the face-centered cubic structure γ(Co–fcc) to the hexagonal close-package ε(Co–hcp) one. Due to the very fine microstructure of the additively manufactured alloy which determines short diffusion paths, only brief soaking times were considered (30, 90, 180 min) to avoid grain coarsening. With the aim to verify the repeatability, heat treatments were performed on all the investigated samples, whose LED was in the optimized range (Table 2).

Phase composition of as-built and heat-treated samples was obtained with X-ray diffraction analyses (XRD, PANalytical Expert PRO with Xcelerator detector) using a Cu Kα radiation source (λ = 0.15406 nm) at 40 mA and 40 kV. Spectra were acquired in 2θ from 30° to 100° with a 0.05° step size and a 15 s dwell time. Phase identification was then performed with the Xpert Highscore Plus software.

A differential thermal analyzer (DTA, Rheometric Scientific STA 1500) was used to perform thermal analyses on the as-built samples. Scans were recorded in the temperature range 30 to 1200 °C by heating specimens of about 100 mg in Ar atmosphere, with a heating rate of 10 °C min^{-1} in an Al_2O_3 crucible. The curves were then elaborated with RSI Orchestrator software.

As a first evaluation of the effect of heat-treatments on mechanical properties, aging curves were obtained by measuring Rockwell hardness (HRC) for all temperature–time combinations.

Metallographic analyses were carried out via optical (OM, Zeiss Imager A1), scanning electron with energy-dispersive X-ray spectroscopy (SEM–EDS, Zeiss EVO 50) and field emission gun scanning electron (FEG–SEM, ZEISS Leo 1530) microscopy on polished and etched surfaces of both heat-treated and as-built samples. The microstructure of samples was characterized on cross sections obtained by cutting samples along the building direction (longitudinal cross section). Surfaces were ground and polished following standard metallographic procedures up to a mirror-finish, then they were electrochemically etched (4 V for 20 s) with an acid ferric chloride solution (5 mL HCl + 10 g $FeCl_3$ in 100 mL aqueous solution [34]). Heat-treated samples in

Table 3 Process parameters adopted for the fabrication of LPBF samples for wear tests and relative density compared to the reference value for the cast alloy [28]

Samples	Laser power [W]	Scanning velocity [mm s^{-1}]	Layer thickness [mm]	Hatching space [mm]	LED [J mm^{-3}]	Density % [–]
L, L-HT	150	1100	0.03	0.06	97	97.8
M, M-HT	130	700	0.02	0.06	155	99.9
H, H-HT	150	500	0.02	0.06	250	99.8

the optimized aging condition were also investigated using Electron Backscatter Diffraction (EBSD) system consisting of a Hikari EBSD camera controlled by EDAX-OIM7.3 equipped in a FEI Quanta 250 FEG–SEM. Different step sizes of 3 µm, 1 µm, 0.5 µm were used. In addition, the as built alloy was investigated using 0.5 µm and 0.05 µm step sizes. The obtained data were post processed using OIM 7.3 EBSD data analysis software.

2.2 Tribological tests

Tribological tests were aimed at comparing the friction and wear behavior of as-built and heat-treated LPBF alloy and a standard block-on-ring contact geometry was chosen for sliding wear test [35]. This geometry clearly does not replicate the complex contact conditions that prostheses experience during in-service life; however, laboratory scale tests (e.g., ball-on-disk and block-on-ring configurations) have been widely adopted in the literature to study the tribological behavior of many metallic biomaterials, including CoCrMo alloys [18]. In fact, the simplified contact geometry allows to directly compare the investigated conditions.

Small bars ($5 \times 5 \times 30$ mm^3) were extracted from the LPBF samples and used as fixed sliders, while an AISI 52100 steel cylinder (40 mm diameter) quenched and tempered to 62 HRC was used as countermaterial. To have a comparison with one of the current standards for implant devices, tribological tests were carried out also on the benchmark ASTM F1537 wrought alloy. The wrought alloy is preferred to the cast one, since, as reported by Hussein et al. [18], forged CoCrMo alloys have higher wear resistance that cast ones, even if they exhibit higher coefficient of friction. Prior to tribological tests, surface roughness and hardness on sliders and cylinder were measured by a stylus profilometer (Hommelwerke T2000, with a tip radius of 5 µm) and by an HRC hardness tester.

The tribological tests were carried out at ambient conditions of humidity and temperature (20–25 °C with a relative humidity ranging from 50 to 60%), at fixed sliding distance and velocity, set at 5000 m and 0.3 ms$^{-1,}$ respectively, and by applying two different normal loads (5 and 10 N), as reported in Table 4. As a line contact is established between the two elements, contact pressures were evaluated according to the Hertzian theory for two cylinders with parallel axes and by imposing an infinite radius to one of the facing body to replicate the block-on-ring contact geometry [36]. According to this theory, the peak contact pressure is defined as the following equation:

$$p_{\max} = (PE^*/\pi R)^{1/2} \tag{1}$$

where P is the normal applied load for unit length, E^* is the contact modulus that considers Poisson ratios and Young modulus of the two facing materials, and R is the reduced radius of contact that considers the radius of both bodies. The mean contact pressure instead is defined as the following equation:

$$p_{\text{mean}} = \pi p_{\max}/4 \tag{2}$$

In the formula, a reference value of 208 GPa for the elastic modulus of AISI 52100 was implemented [37]. For the LPBF CoCr alloy, instead, the elastic modulus was experimentally measured on as-built samples via a non-destructive ultrasonic method, whose principle is described in the literature [38], giving an average value of 239.5 ± 11.5 GPa. The estimated contact pressures are reported in Table 4. During the tests, friction force was continuously measured by means of a load bending cell. Coefficient of Friction (COF) values were then averaged over the steady-state regime for each test, set at 500–5000 m range. Wear scar dimensions on sliders, in term of depth, were characterized by stylus profilometry and worn surfaces were investigated by 3D-digital microscopy (Hirox KH-7700) and SEM–EDS to identify the main wear mechanisms. Furthermore, worn tracks on sliders were investigated also by µRaman spectroscopy to identify the oxide layers formed during the tribological contact. For this purpose, a Renishaw InVia micro-spectrometer equipped with a Leica DMLM microscope was used, operating with a 50 mW Ar^+ laser (wavelength: 514.5 nm).

3 Results

3.1 Aging treatment assessment

XRD and thermal analyses (Fig. 1) were performed to assess changes occurring in the phase composition of the alloy due

Table 4 Wear tests conditions and calculated Hertzian contact pressures

Sliders	Applied normal load [N]	Sliding distance [m]	Sliding velocity [m s^{-1}]	p_{max} [MPa]	p_{mean} [MPa]	Countermaterial
L, L-HT M, M-HT H, H-HT Wrought alloy	5; 10	5000	0.3	44; 62	35; 49	AISI 52100

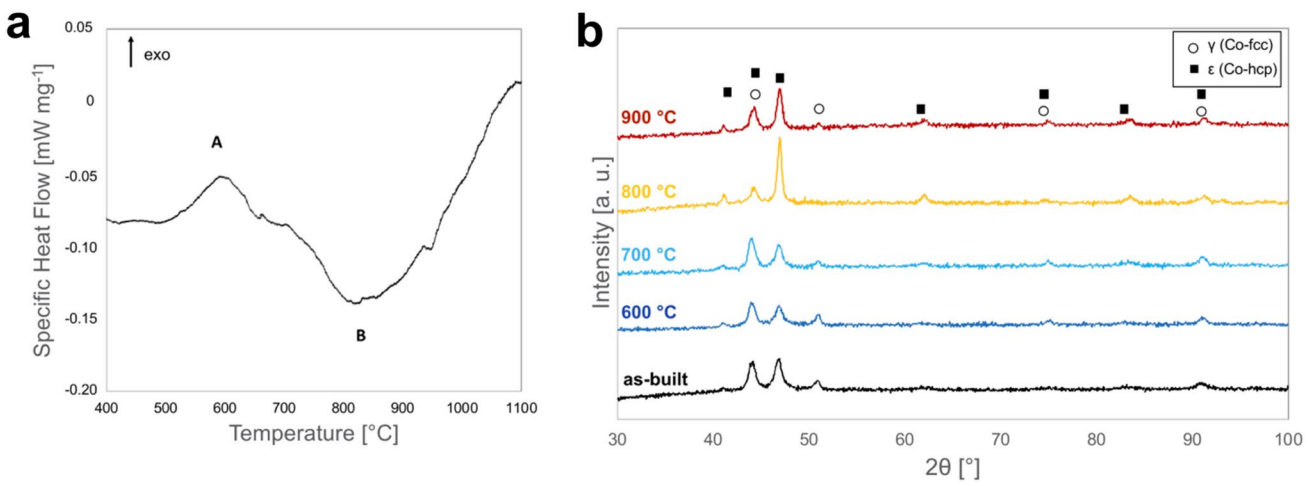

Fig. 1 Microstructural characterization: **a** differential thermal analysis (DTA) on the LPBF as-built Co28Cr6Mo alloy, where "A" defines the γ(Co–fcc) to ε(Co–hcp) phase transformation and "B" the ε(Co–hcp) to γ(Co–fcc) one; **b** phase composition (XRD) analyses on as-built and heat-treated samples aged for 180 min at 600, 700, 800 and 900 °C

to high temperature exposure. The differential thermal analysis (DTA) of the as-built LPBF alloy (Fig. 1a), showed an exothermic peak (A) located at about 600 °C followed by an endothermic peak (B) around 830 °C, both related to the allotropic γ(Co–fcc) to ε(Co–hcp) transformation. Specifically, the exothermic peak (A) is related to the γ → ε transformation, while the endothermic peak (B) to the following ε → γ transformation. The literature [39] confirms that peak A is located at about 600 °C, while peak B is usually located at 950 °C. Peak B in the present study is moved to a lower temperature, suggesting that the change from hcp to fcc phase is anticipated. It can be inferred that a modification in the kinetics of the transformation occurred, as also observed for other LPBF alloys [12, 40], presumably due to the extremely fine microstructure. By recalling the binary Co–Cr phase diagram [9], ε(Co–hcp) is the equilibrium phase at room temperature and the transformation to the γ(Co–fcc) phase occurs in the range 900–950 °C. However, the presence of both ε and γ phases in the LPBF as-built alloy was already evidenced in the literature [32, 41, 42] and can be explained by the high cooling rates developed during LPBF and the resulting small grain size that hinder the γ → ε transformation that, even in equilibrium conditions, is not kinetically favored. In fact, according to the XRD spectra (Fig. 1b), in the as-built alloy both ε(Co–hcp) (ICDD:5–727) and γ(Co–fcc) (ICDD:15–806) Co-phases were present.

By comparing XRD spectra of as-built and heat-treated for 180 min alloys (Fig. 1b), the occurrence of the fcc → hcp transformation (peak A in DTA analysis) due to the high temperature exposure, was confirmed. In the spectra, ε(Co–hcp) and γ(Co–fcc) reflections are often overlapped; however, by focusing on the peaks related only to the ε phase (located approximately at 2θ = 41.4°, 47°, 62.5°, 83.8°) it is possible to observe that their intensity increases with increasing temperature, especially for 800 and 900 °C treatments. Concurrently, peaks related to the sole γ phase progressively decrease their intensity. Therefore, by increasing the treatment temperature, the fcc → hcp transformation was promoted.

The modifications in the microstructure induced by aging treatments are shown in Fig. 2, where the as-built condition is compared to low (750 °C) and high temperature (850 and 900 °C) ones, for a soaking time of 180 min. The LPBF process of the Co28Cr6Mo results in a hierarchical microstructure, consisting of subsequent layers composed by solidified melt pools, long epitaxial grains parallel to the building direction that cross-over layers, and a cellular submicrometer sized structure appreciable only at high magnifications. In Fig. 2, boundaries of solidified melt pools are underlined by yellow dashed lines, epitaxial grains by orange dashed lines and the fine cellular structure by solid green lines. In the optical micrograph of the as-built alloy (Fig. 2a), solidified semi-circular melt pools typical of LPBF components can be clearly identified. Cellular sub-structure can be instead resolved at high-magnification SEM analyses (Fig. 2e).

After the heat treatment, melt pool boundaries became less clear (Fig. 2b, c), even if the layered microstructure due to the additive process can be still recognized. Microstructural analyses showed the development of new microstructural features that initially involved boundaries of the aforementioned long epitaxial grains (Fig. 2b, f) and, with increasing temperature, affected the whole microstructure (2c, d). Cellular sub-structure underwent a progressive break down (Fig. 2g, h), forming globular particles finely distributed in the matrix. As also reported in case of LPBF Al–Si

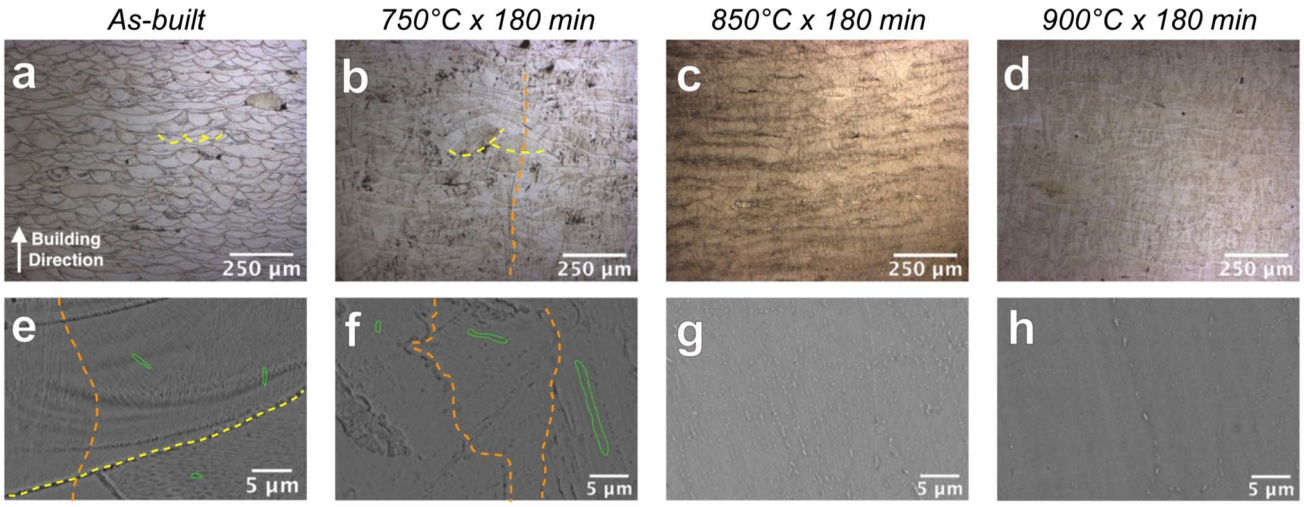

Fig. 2 Microstructural characterization of LPBF Co28Cr6Mo in the as-built condition (**a**, **e**) and heat treated for 180 min at 750 °C (**b**, **f**), 850 °C (**c**, **g**), and 900 °C (**d**, **h**). Micrographs **a**–**d** were obtained by OM, while **e**–**h** by SEM. Yellow and orange dashed lines underline boundaries of solidified melt pool and epitaxial grains, respectively. Green solid lines underline cellular structure

alloys [11, 12], due to the high-temperature exposure the fine cellular structure evolved in globular particles that, due to the relative short soaking time, preserved a sub-micrometer size. Globular particles reached their maximum density in the alloy heat-treated at 850 °C for 180 min (Fig. 2g), while, after aging at 900 °C for 180 min (Fig. 2h), globular particles were partially dissolved.

The change in hardness as a result of the exposure time at high temperatures is shown in Fig. 3, where aging curves obtained for all heat-treated samples are reported and compared to the hardness of the as-built LPBF alloy (black dashed line).

Presumably as a result of the progressive $\gamma \rightarrow \varepsilon$ and the concurrent evolution in the microstructural features, all treatments promoted a strengthening of the alloy. In particular, aging at low temperatures (600–750 °C) resulted in a progressive and moderate hardness increase (from 37 HRC of the as-built alloy to a maximum of 40 HRC). The greatest strengthening was reached at 800–850 °C, with a progressive hardness increase till the value of 47 HRC after the 180 min treatment. By recalling microstructural analyses, in these conditions it was also observed the maximum density of finely dispersed globular particles. On the other hand, aging at 900 °C induced an initial increase in

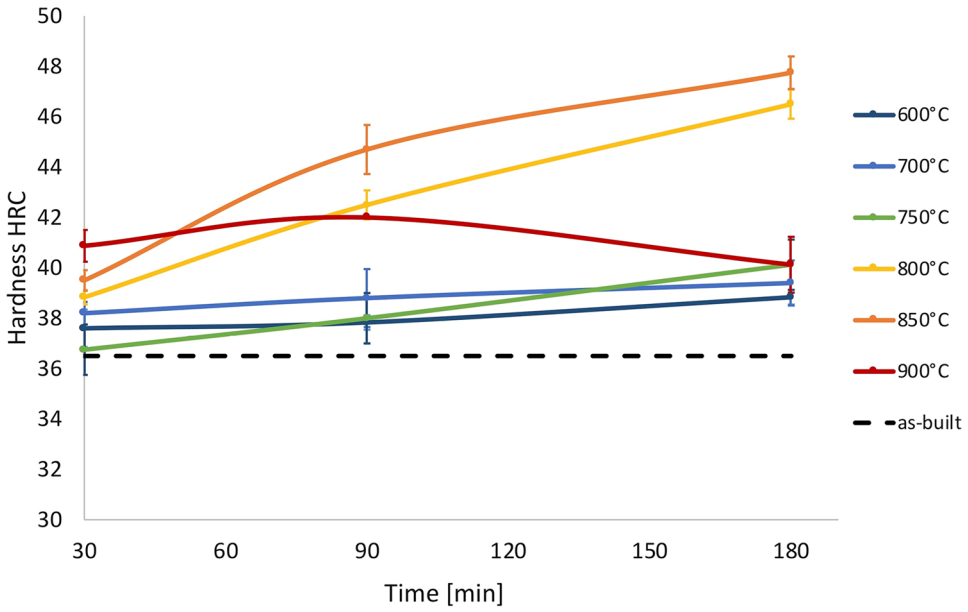

Fig. 3 Aging curves for the LPBF Co28Cr6Mo alloy

hardness (approx. 42 HRC after the 30 and 90 min treatment) that, after the 180 min treatment, dropped to 40 HRC possibly as a consequence of the partial dissolution of globular particles.

3.2 Optimized heat-treated condition

For the purpose of the present study, the optimized heat-treated condition was found in the 850 °C for 180 min, that resulted in the highest hardness increase due to the $\gamma \rightarrow \varepsilon$ phase transformation and the complete modification of the microstructural features induced by LPBF. Therefore, further microstructural analyses were carried out in the alloy aged in this condition. FEG–SEM analyses (Fig. 4) confirmed that microstructural features peculiar of the as-built LPBF Co28Cr6Mo alloy, such as well-defined melt pool boundaries and cellular microstructure (Fig. 4a), were no longer present after the optimized heat treatment (Fig. 4b). In fact, the heat-treated alloy evidenced the aforementioned fine globular particles densely distributed in the matrix. These particles were not randomly oriented, but they followed the orientation of epitaxial grains, as evidenced by the orange dashed lines in both figures. Further analyses at higher magnification showed that globular particles (Fig. 4d) were much smaller than the original cellular structure of the as-built alloy (Fig. 4c) and, specifically, their size mainly lied in the range 100–200 nm. Presumably, as already discussed, these globular particles originated from the cellular structure as a consequence of the breakdown of the fine network formed by cell boundaries, following the mechanism reported in Fig. 5. This assumption was also supported by EDS analyses, reported in Fig. 6, where the semi-quantitative chemical composition of cells core and boundaries in the as-built alloy was compared to globular particles and Co matrix of the aged alloy. If compared to the cells core and Co matrix (Spectra 1), both cell borders and globular particles evidenced an enrichment in Mo, Si and C. Segregation of alloy elements in correspondence of cell borders, especially Mo in case of CoCrMo alloys, is confirmed by previous papers [7, 43–45], and was also often reported for others metals subjected to LPBF; the reasons lie in the complex physical and chemical mechanisms occurring during rapid solidification conditions.

The grain structure of the optimized sample has been investigated using EBSD with different step sizes. Figure 7 shows the inverse pole figure (IPF) coloring maps and grain

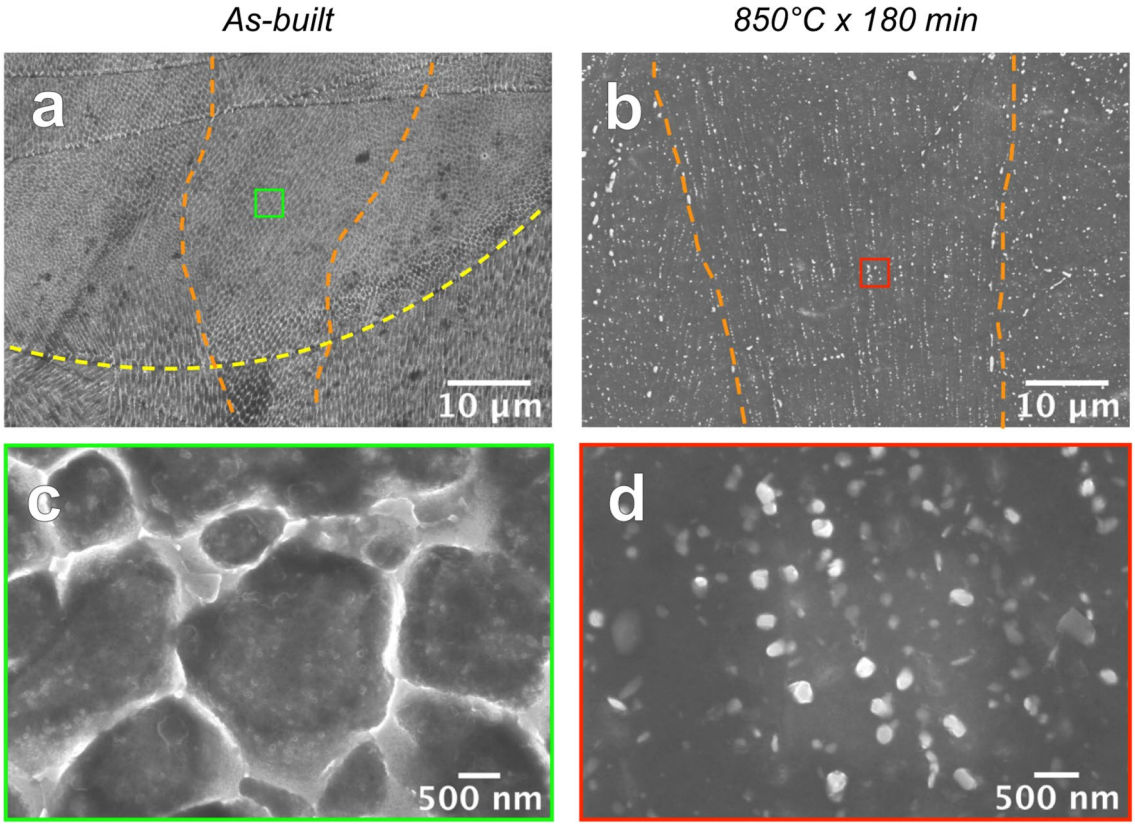

Fig. 4 FEG–SEM microstructural analysis on: **a**, **c** as-built and **b**, **d** heat-treated at 850 °C for 180 min Co28Cr6Mo LPBF alloy (optimized heat-treated condition). In low magnification analyses (**a**, **b**) yellow and orange dashed lines underline boundaries of solidified melt pool and epitaxial grains, respectively. In high magnification micrographs (**c**, **d**) detail of cellular sub-structure (green frame) and globular particles (red frame) is given

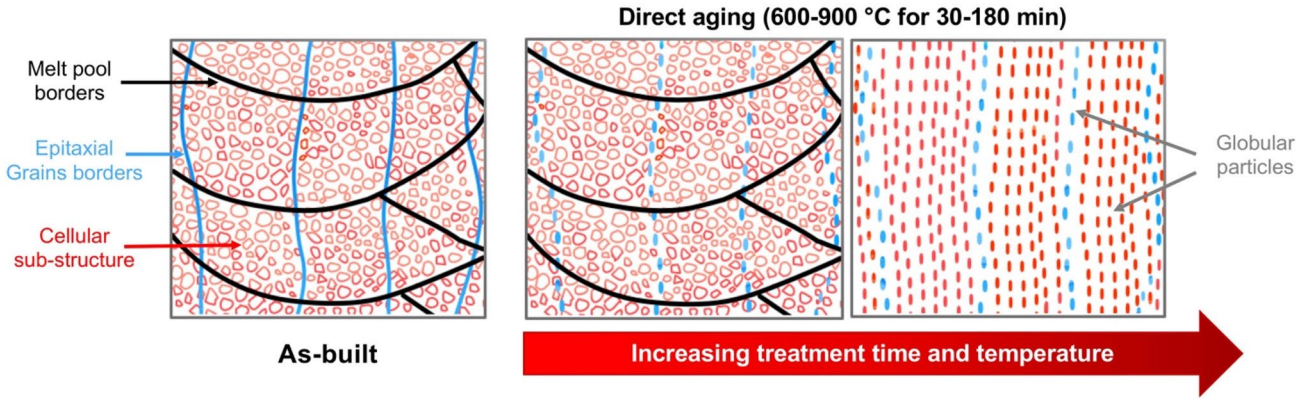

Fig. 5 Schematic representation of the modifications occurring in the cellular sub-structure of LPBF Co28Cr6Mo alloy after direct aging treatment

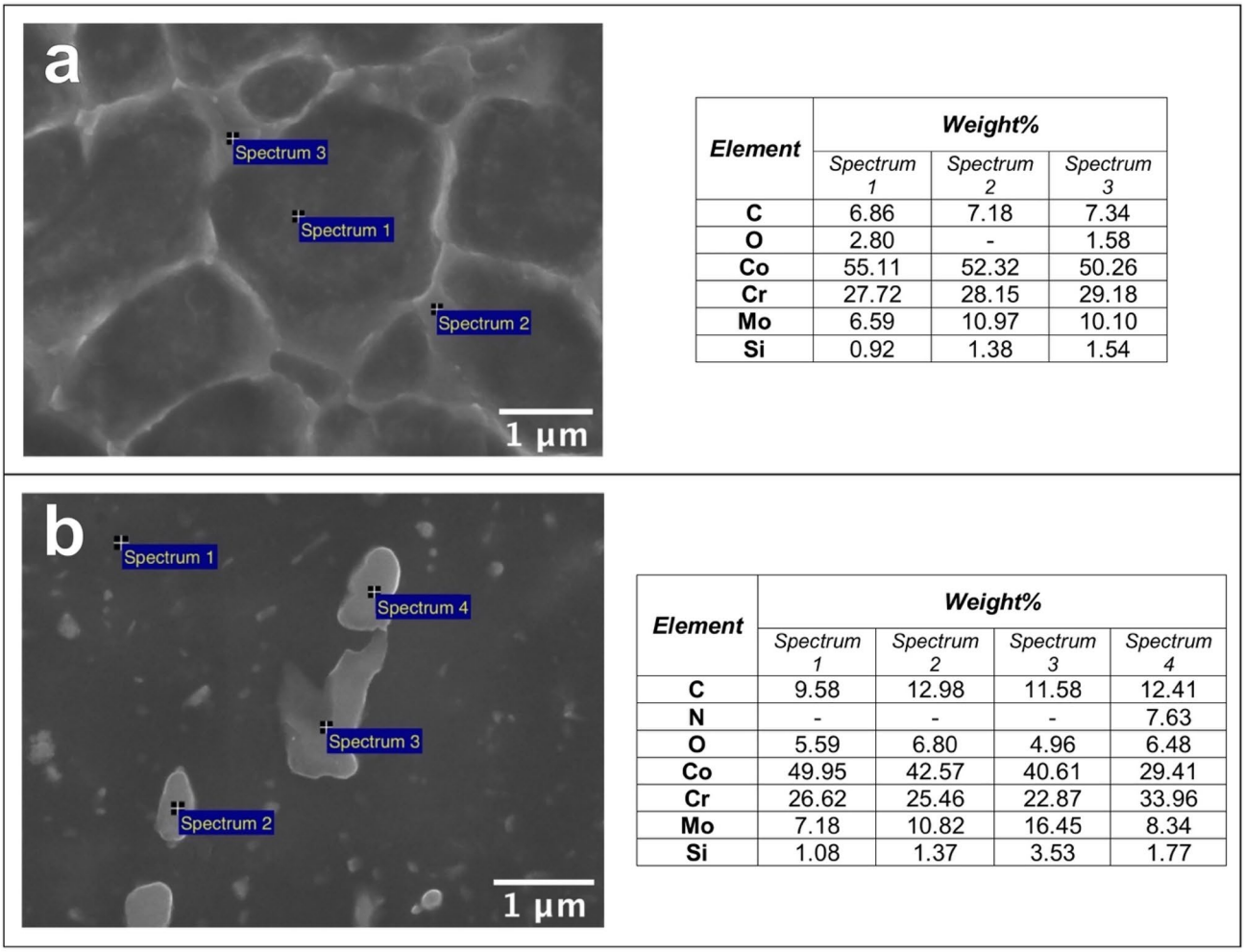

Element	Weight%		
	Spectrum 1	Spectrum 2	Spectrum 3
C	6.86	7.18	7.34
O	2.80	-	1.58
Co	55.11	52.32	50.26
Cr	27.72	28.15	29.18
Mo	6.59	10.97	10.10
Si	0.92	1.38	1.54

Element	Weight%			
	Spectrum 1	Spectrum 2	Spectrum 3	Spectrum 4
C	9.58	12.98	11.58	12.41
N	-	-	-	7.63
O	5.59	6.80	4.96	6.48
Co	49.95	42.57	40.61	29.41
Cr	26.62	25.46	22.87	33.96
Mo	7.18	10.82	16.45	8.34
Si	1.08	1.37	3.53	1.77

Fig. 6 FEG–SEM EDS localized semi-quantitative analysis on: **a** as-built and **b** heat-treated at 850 °C × 180 min (optimized heat-treated condition) Co28Cr6Mo LPBF alloy

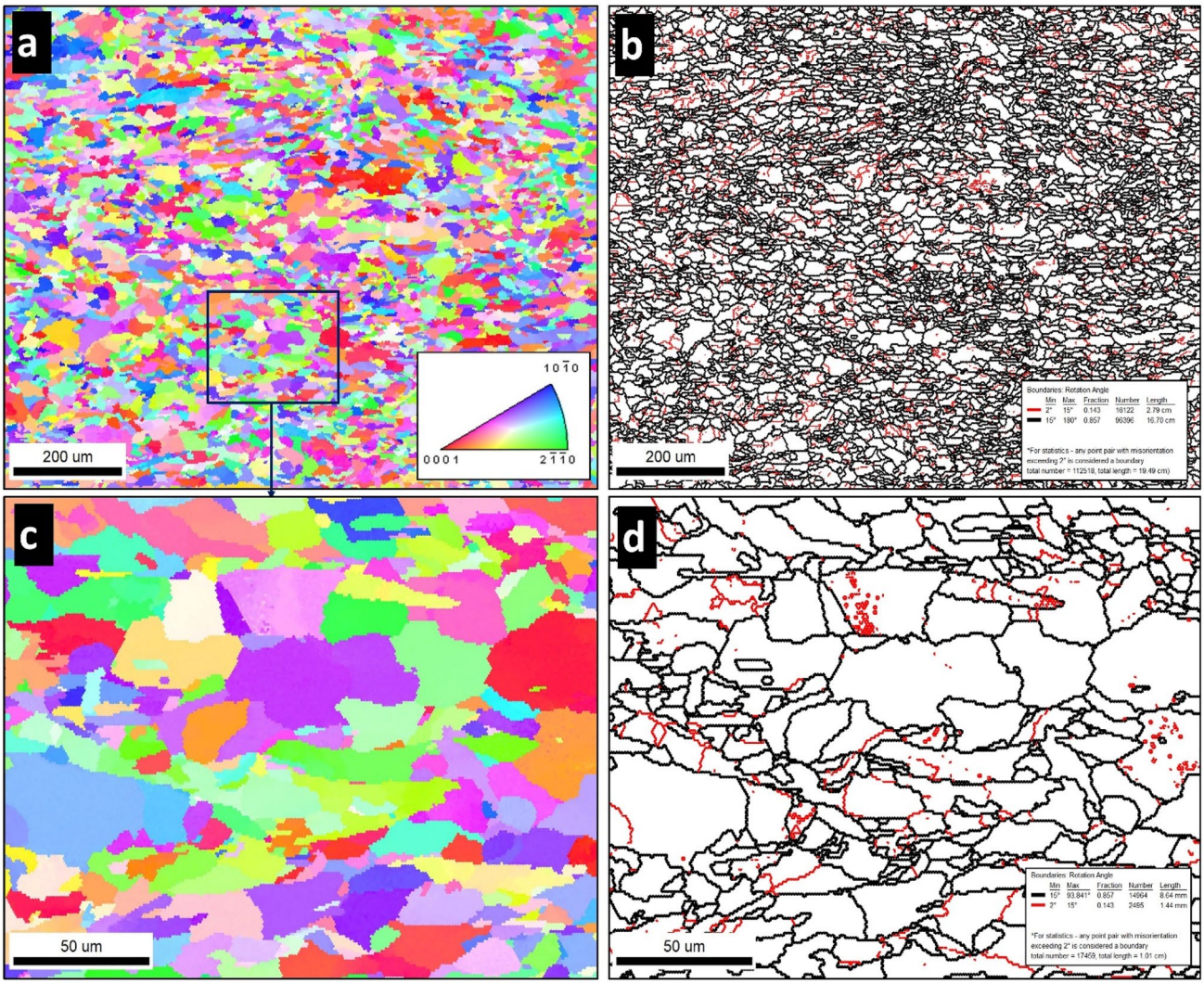

Fig. 7 Inverse pole figure (IPF) maps and Grain boundary maps with high angle boundaries (HABs) in black lines and low angle boundaries (LABs) in red lines for the Co28Cr6Mo LPBF alloy after the optimized heat treatment: **a**, **b** EBSD data collected using 3 µm step size and **c**, **d** EBSD data obtained using 1 µm step size at the rectangle indicated in (**a**). Coloring keys for the IPF maps and GB maps are given on the maps

boundary maps, where high angle boundaries (HABs) are in black lines and low angle boundaries (LABs) are in red lines. Maps have been generated from EBSD data acquired using 3 µm step size in case of Fig. 7a, b 1 µm step size in Fig. 7c, d. Data reported in Fig. 7c, d refer to the area indicated by the rectangle in Fig. 7a. The grain orientation can be considered random with mixed (0001)/red, $(10\bar{1}0)$/ blue and, $(2\bar{1}\bar{1}0)$ /green orientations, as it can be observed from IPF maps. This implies random nucleation upon recrystallization. In addition, it can be observed that the microstructure after the heat treatment was recrystallized, with irregular grain morphologies and wide range grain sizes. The average grain size calculated for the EBSD data acquired using 3 µm step size (Fig. 8a) was about 14 µm and that for the data acquired using 1 µm step size (Fig. 8d) was about 9 µm as it can be observed from the grain size distribution histograms in Fig. 8a, d, respectively. This difference in grain size is mainly due to the use of large step size, as the 3 µm step during EBSD data acquisition does not detect the grains smaller than 3 µm with any point of indexing. This eliminated all the small grains from the calculations. The grain size distributions also indicated the wide range of the grain size from about 3 µm to about 60 µm. In terms of grain boundary structure, the microstructure mainly consisted of high angle boundaries (black lines) that represented about 86%, with some low angle boundaries (red lines) that represented about 14% in a form of substructure, as can be noted from the grain boundary maps in Fig. 7b, d. In addition, it can be observed that a large number of grains are completely free of substructure due to recrystallization process that occurred upon heat

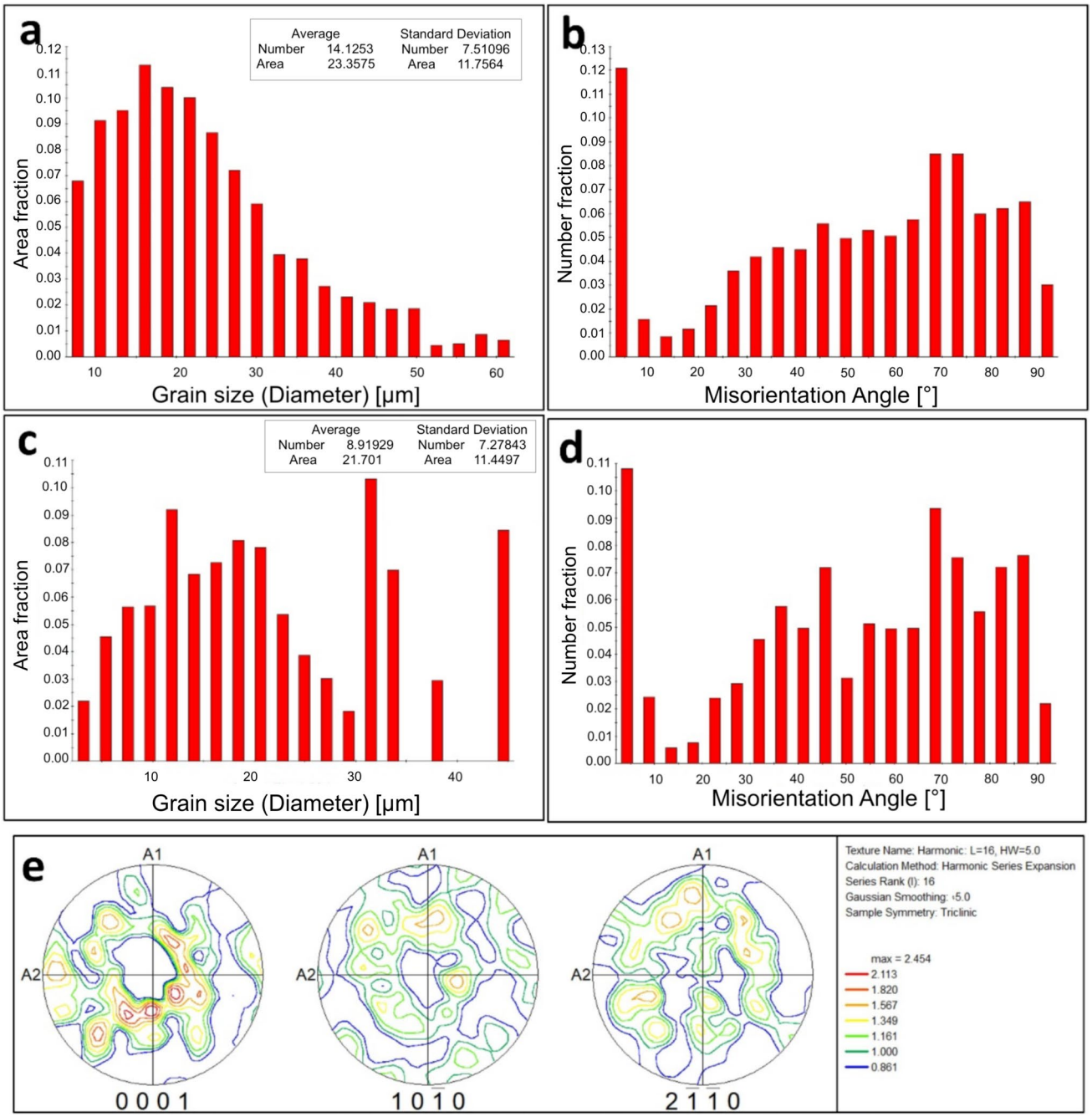

Fig. 8 Grain size and misorientation angle distributions (calculated from the data in Fig. 7): **a** and **b** EBSD data collected using 3 μm step size; **c** and **d** EBSD data obtained using 1 μm step size; **e** pole figures (PFs) calculated from the data in Fig. 7a

treatment. However, still few substructures can be observed which might be due to the transformation of the γ(Co–fcc) into ε(Co–hcp) phase during the heat treatment process, as also observed in the aged CoCrWMo LPBF alloy [46]. The misorentation angle distributions shown in Fig. 8c, d also indicated the dominance of the HABs in the range from 15 to 90° with only few amount of LABs. This confirmed the static recrystallization that occurred upon the heat treatment.

From the analysis of pole figures in Fig. 8e, a weak recrystallization texture can be noticed, with only about 2 times random. This is in agreement with the random orientation observed in the IPF maps. It should be mentioned here that the material after heat treatment has only the ε(Co–hcp) phase, as also suggested by the previously discussed XRD and DTA analyses.

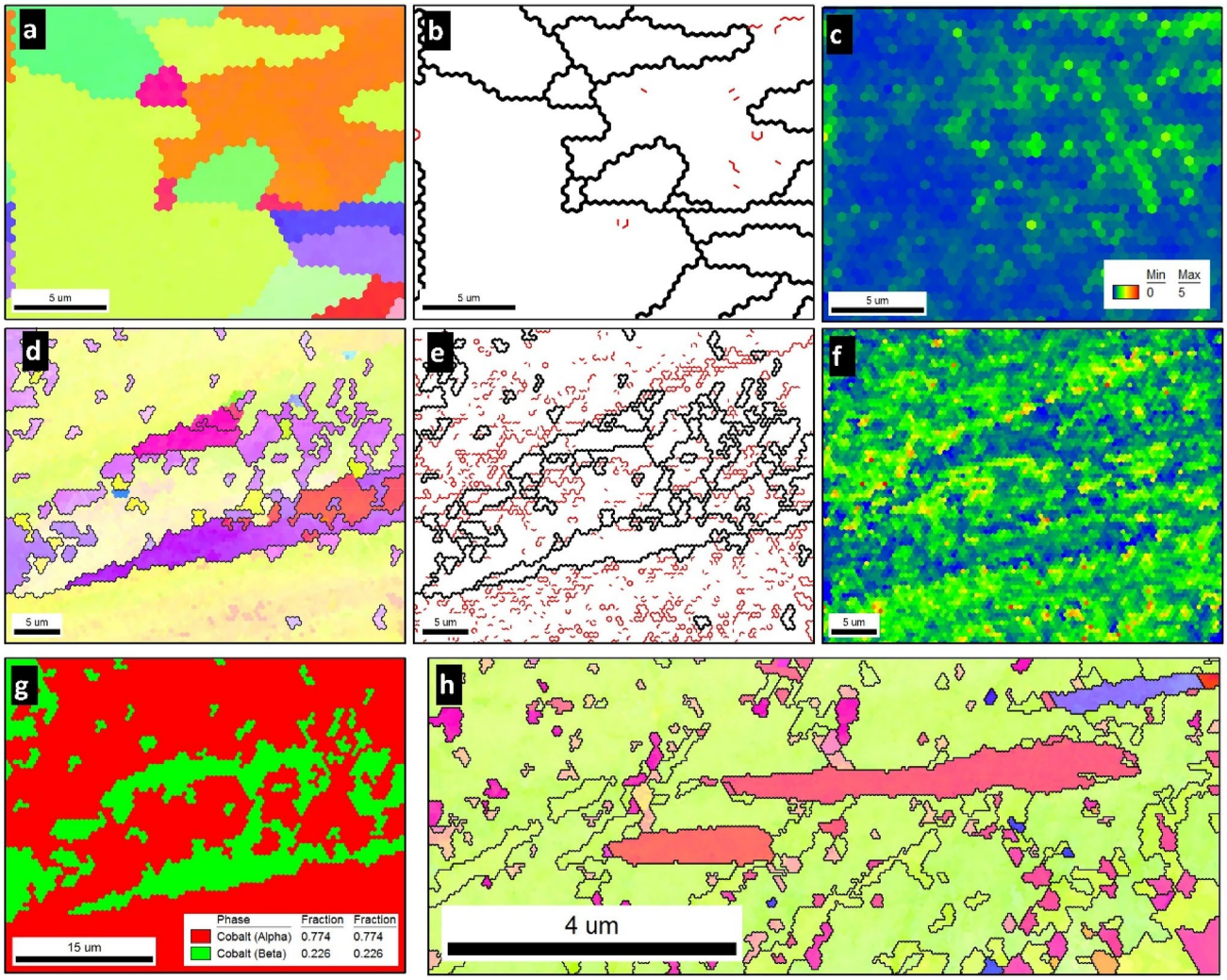

Fig. 9 High resolution EBSD data with different type of maps: **a**, **b** and **c** IPF, GB and Kernal average misorentation (KAM), respectively, for the optimized heat-treated alloy obtained using 0.5 µm step size; **d**, **e**, **f** and **g** IPF, GB, KAM and phase map, respectively, for the as-built alloy obtained using 0.5 µm step size; **h** IPF with GB map superimposed obtained using 0.05 µm from the as-built alloy. In figure **g** Cobalt(Alpha) refer to ε(Co–hcp) and Cobalt(Beta) to γ(Co–fcc)

To further investigate the microstructural features after aging treatment and to compare them with that of the as-built alloy, high resolution EBSD data were acquired using 0.5 µm step size in both alloy conditions and, for the as-built material, further data were acquired with 0.05 µm step. Figure 9 shows the IPF, grain boundaries (GB) and kernel average misorientation (KAM) maps for both alloy conditions: Fig. 9a–c refers to the heat-treated alloy, while Fig. 9d–f to the as-built one. From these analyses, the following differences in the microstructural features of the as-built alloy, if compared to the heat-treated one, can be summarized: (i) it has higher density of LABs (approx. 46 vs 5% at this level of resolution); (ii) it has higher density of dislocation due to the fast cooling during LPBF and this can be clearly observed from the KAM map of the as-built alloy with very high density of average misorientation (Fig. 9f) compared with that of the heat treated alloy (Fig. 9c); (iii) it has ultra-fine sub-structure to the level of sub microns (about 0.3 µm average grain size) relative to about 4 µm average grain size for the heat-treated alloy at this high level of resolution; iv) it consists of a two phases structure with a predominance of the ε(Co–hcp) phase (about 70%) as it can be observed from the phase map of the as-built alloy in Fig. 9g.

3.3 Wear behavior

Dry sliding wear tests were carried out on the LPBF Co28Cr6Mo alloy both in the as-built and optimized heat-treated condition (850 °C × 180 min), and the conventional wrought forged alloy was used as benchmark. The aim was

to investigate the effect of hardness increase in the friction and wear behavior. In addition, also the effect of different process parameters was considered by testing samples obtained with very different LED values (Table 3). Before tests, both sliders and countermaterial were characterized in terms of hardness and surface roughness (Table 5). As for the latter, the same surface finishing was assured for all LPBF Co28Cr6Mo sliders (Ra = 0.22 ± 0.02 µm), while the steel cylinder was polished to a final surface roughness Ra = 0.13 ± 0.02 µm. Regarding hardness, in the as-built condition the slider processed with low LED (L) was characterized by a lower hardness (29 HRC) than slider obtained at high (H) and medium LED (M), whose hardness was comparable and approximately equal to 36 HRC. This result can be explained with the higher porosity content of low LED samples, with respect to medium and high LED samples that are characterized by a near-full density, as reported in Table 3. After heat treatment, M-HT exhibited the highest hardness among all the tested samples and confirmed the value of 47 HRC discussed in Sect. 3.1 for samples obtained in a comparable LED range. However, it should be noticed the greatest hardness increase due to heat treatment, by comparison with the as-built condition, where recorded by sliders obtained in the low LED range (L-HT) that raised from 29 to 42 HRC, while the high LED sliders (H-HT) exhibited the lowest hardness increase, passing from 35 to 44 HRC. The conventional wrought alloy, instead, was characterized by a hardness value of 39 HRC, consistent with a hot forging process [29]. Hardness of the quenched and tempered bearing steel used as countermaterial was equal to 62 HRC, thus higher than those of all the tested sliders made of the alloy under investigation.

Results of the wear tests in terms of steady-state coefficient of friction (COF) and maximum wear scar depth (WD) measured on sliders at the end of the tests, are reported in Fig. 10. Values measured on the LPBF samples produced in different processing conditions, in terms of LED, both in the as-built and heat-treated condition are compared at 5 (Fig. 10a) and 10 N (Fig. 10b) normal load. The wrought alloy was considered as benchmark.

As far as the lowest load is considered (Fig. 10a), the average COF ranged between 0.5 and 0.95 for all tested samples, with the maximum values recorded in case of L and conventional wrought alloy samples. By considering the effect of LED in the as-built alloy, the lowest COF was recorded in case of M samples, however, after the heat treatment the influence of LED was almost negligible. Moreover, the COF generally decreased after the heat treatment. In a few cases (L and M-HT samples) the standard deviation (SD) was considerable. It was probably a consequence

Table 5 HRC hardness and surface roughness (R_a, µm) of Co28Cr6Mo sliders (as-built and aged (HT)) and steel cylinder used for wear tests. Samples were fabricated with low (L and L-HT), medium (M and M-HT), and high (H, H-HT) LED values, as reported in Table 3

	Sliders							Cylinder
	L	L-HT	M	M-HT	H	H-HT	Wrought alloy	
HRC	29 ± 1	42 ± 2	36 ± 1	47 ± 1	35 ± 2	44 ± 2	39 ± 1	62 ± 1
Ra [µm]	0.22 ± 0.02							0.13 ± 0.02

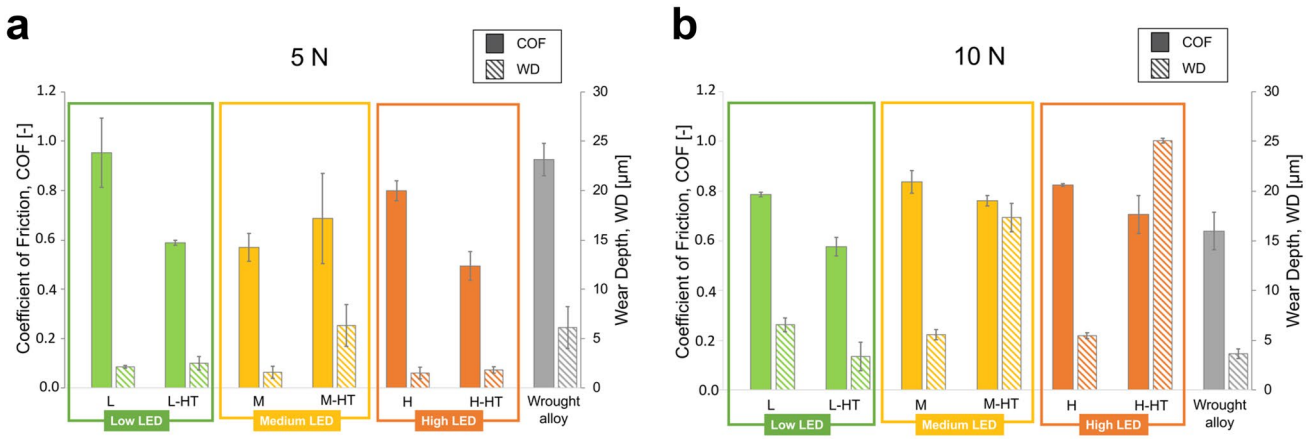

Fig. 10 Wear tests results in terms of COF (solid bars) and WD (dashed bars): **a** 5 N tests, **b** 10 N tests. Results are compared for all the investigated LED values for the as-built (L, M, H) and heat-treated alloy at 850 °C for 180 min (L-HT, M-HT, H-HT). The conventional wrought alloy (hot forged) is used as benchmark

of stick–slip phenomena occurring during sliding at low normal load, especially in case of M-HT samples that, as will be later explained, suffered adhesive wear. In fact, this aspect was less marked in the test performed at 10 N. It should also be considered that L samples were characterized by a low density (Table 3). Therefore, defects such as lacks-of-fusion present on the surface may have affected the frictional behavior (COF and SD values) and the formation of the thick, protective and compact oxide layer, discussed further below, when tested at lower load.

In terms of wear behavior, the wear resistance of all LPBF as-built sliders was higher than that of the conventional wrought one. Neither LED or heat treatment affected the wear resistance of the LPBF alloy, with the only exception of M-HT samples, that exhibited an increased WD by comparison with the untreated (M). However, even in this case wear resistance was higher than the wrought alloy. This is a remarkable result, since the mean contact pressure experienced by prosthetic implants during service life *in-vivo* conditions is in the range of 10–30 MPa with occasional peaks up to 50 MPa [47, 48], thus this condition is better represented by 5 N tests (Table 4).

By increasing the applied load to 10 N (Fig. 10b), in case of LPBF alloy the COF generally increased or was little affected by normal load (also taking into account the SD), while the wrought alloy showed an opposite trend, with a COF reduction from 5 to 10 N normal load. Result showed no significant influence of both LED and heat treatment in the frictional behavior of LPBF alloy tested at 10 N. As concerning the wear behavior, it is worth noticing that wear damage of the LPBF processed alloy was still comparable with that of wrought alloy, with the only exception of the heat-treated M and H samples tested at 10 N. All LPBF processed samples both as-built and heat-treated, showed increased wear scar depths, with increasing load; an opposite trend was instead recorded in case of the wrought alloy. The effect of heat treatment was not obvious, and not directly related to the hardness values, since it produced different outcomes on the basis of LED values. For low LED samples (L), the heat treatment succeeded in improving the wear resistance, especially at 10 N applied load. For medium and high LED samples, the wear resistance was drastically reduced after heat treatment. However, it should be also mentioned that contact pressures reached in 10 N tests are considerably high and, by referring to orthopedic implants, they will be hardly reached during in-service conditions.

The characterization of wear scars of the LPBF alloy performed by means of 3D-digital microscopy and SEM–EDS analysis, reported in Fig. 11, allowed the identification of the different wear mechanisms occurring during the tests, synthesized in Table 6. Two main wear mechanism were identified, typical of sliding conditions: (i) a mild-oxidative wear regime, experienced by the majority of sliders (Fig. 11a, b, d, e); (ii) a severe adhesive wear regime (Fig. 11c, f). Mild-oxidative wear regime resulted in the low wear damage of the sliders in the reason of the formation

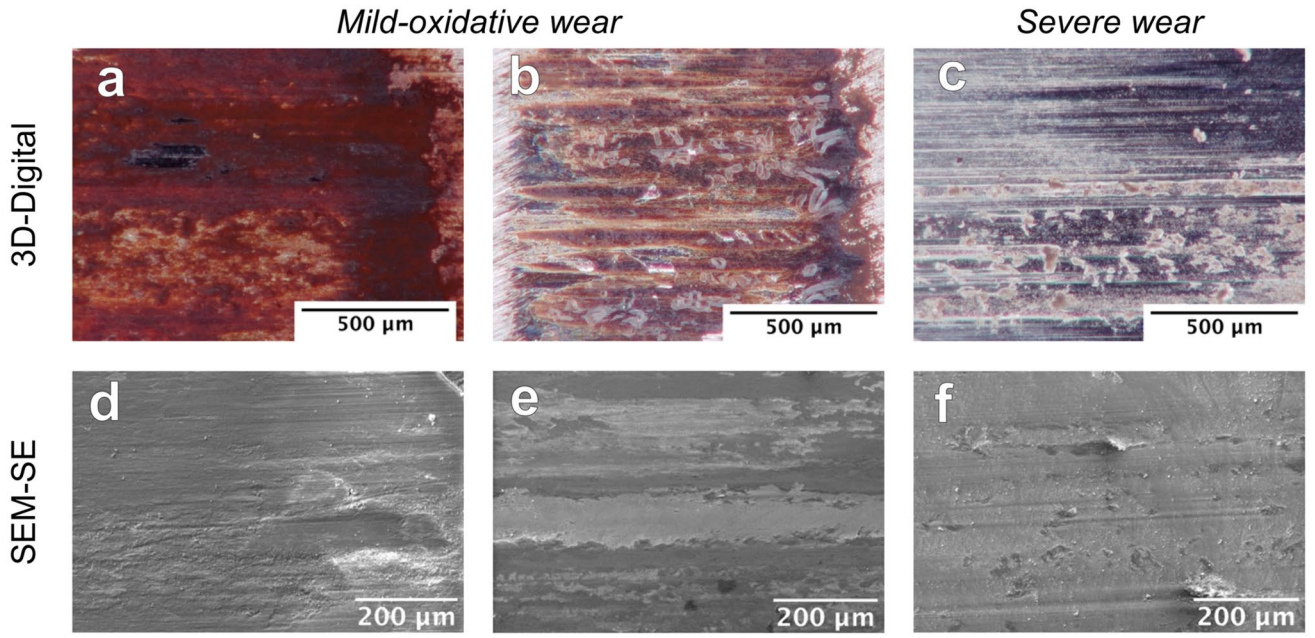

Fig. 11 Analyses on representative wear scars performed by 3D-digital microscopy and SEM showing the different wear mechanisms occurring in LPBF samples: **a** and **b** mild-oxidative wear at 5 N; **d** and **e** mild-oxidative wear at 10 N; **c** and **f** severe wear. In Table 6, wear regimes of all tested conditions are summarized

Table 6 Summary of wear regimes established during wear tests, as a function of LED range, heat-treatment condition and applied normal load

Samples	Heat treatment	LED range	Normal Load [N]	Wear regime	
				Mild-oxidative	Severe adhesive
L	No	Low	5	✓	
			10	✓	
L-HT	Yes		5	✓	
			10	✓	
M	No	Medium	5	✓	
			10	✓	
M-HT	Yes		5		✓
			10		✓
H	No	High	5	✓	
			10	✓	
H-HT	Yes		5	✓	
			10		✓

Representative wear scars associated to mild-oxidative and severe adhesive wear regime are reported in Fig. 11

of a protective oxidative tribo-film between the sliding surfaces of both sliders and cylinder. The occurrence of this wear mechanism is also confirmed by the COF value in the range 0.5–0.8 that typically corresponds to the sliding contact between iron oxides [49, 50]. On the other hand, the adhesive/delamination wear regime established during wear tests is responsible for the higher wear scar depths measured in case of M-HT and H-HT samples. Micrograph in Fig. 11 also evidenced two different wear behavior in case of mild-oxidative wear: (i) in case of 5 N tests, a thick and compact reddish layer was formed (Fig. 11a, d), (ii) for 10 N tests the layer was thinner, darker and did not homogeneously cover the scar (Fig. 11b, e). This outcome was also confirmed by EDS maps and Raman analyses performed on wear scars (Fig. 12). EDS maps, in fact, revealed a layer of iron-based oxides, thicker in case of tests performed at 5 N (Fig. 12a) than 10 N (Fig. 12c). For severe wear regime, instead, the worn surfaces were almost free of this protective oxide layer (Fig. 12e). Furthermore, according to Raman analyses, the oxide layer formed in case of 5 N (Fig. 12b) was mainly composed by hematite (Fe_2O_3), while the increase to 10 N led to the formation of magnetite (Fe_3O_4) [51–53].

It is worth noticing that the wear resistance does not reflect the hardness increase induced by aging treatment in the LPBF processed alloy (Table 5). In fact, the maximum wear scar depths (minimum wear resistance) were recorded in the heat-treated M and H samples, despite their superior hardness values, equal to 47 and 44 HRC, respectively. According to the Archard's law (3) for sliding wear of metals [54], in fact, the wear rate (W, defined as the ratio between the wear volume V and the sliding distance S) is directly related to the applied load (F) and the sliding distance (S). On the contrary, it is inversely related to the alloy hardness

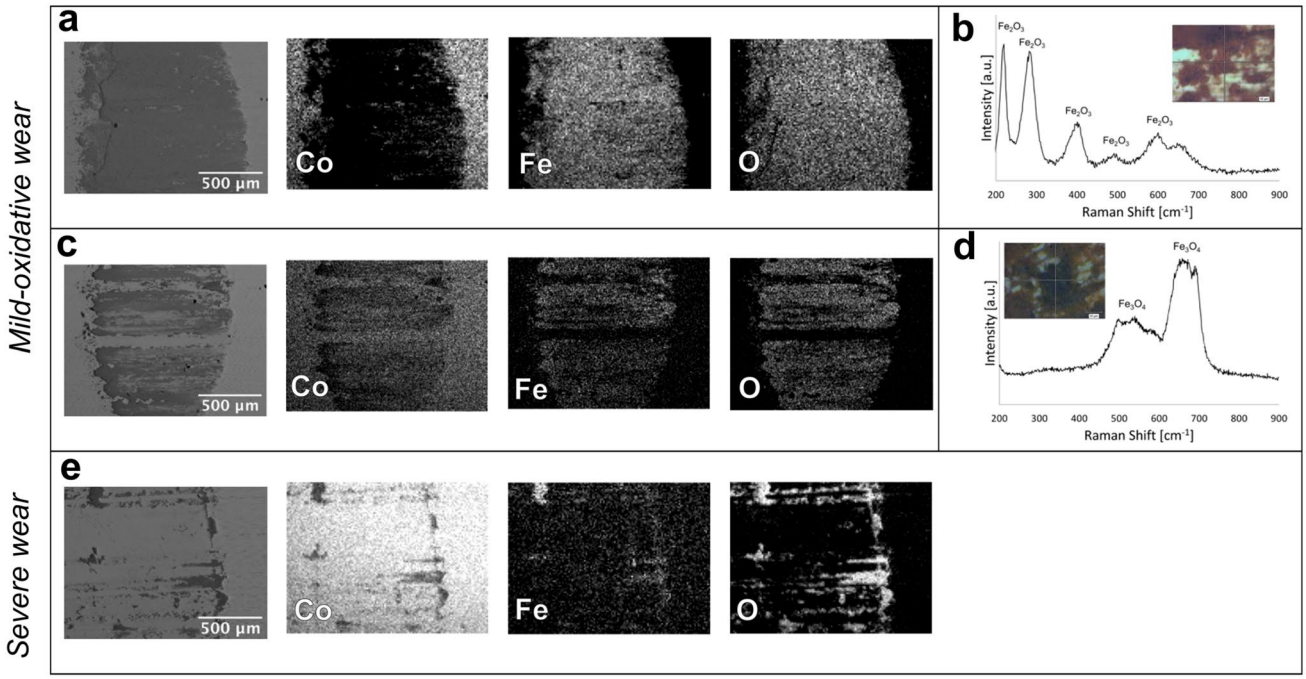

Fig. 12 SEM–EDS maps of wear scars on LPBF alloy for: **a** and **c** mild-oxidative regime at 5 N and 10 N, respectively; **e** severe wear regime. Raman analyses for mild-oxidative regime at: **b** 5 N and **d** 10 N

(H); thus, for a high hardness value a corresponding high wear resistance should be expected. In (3), the term k' is the Archard wear coefficient.

$$W = \frac{V}{S} = k' \cdot \frac{F}{H} \tag{3}$$

However, as reported in [55, 56] with increasing hardness, also fracture toughness has an important role in the sliding wear behavior. In fact, the decrease in fracture toughness, generally induced by an increased alloy hardness, can lead to different wear mechanisms, involving microcracking and consequent formation of highly abrasive wear debris. The wear rate in this case is inversely proportional to both fracture toughness (Kc) and hardness (H), and increases more than linearly with the applied load, as reported in (4) [56].

$$W \propto \frac{F^{\frac{9}{8}}}{K_c^{\frac{1}{2}} \cdot H^{\frac{5}{8}}} \tag{4}$$

Therefore, in case of the heat-treated alloy the increased wear rate is presumably related to the transformation into the ε(Co–hcp) phase, that is characterized by a greater hardness than γ(Co–fcc) and a lower fracture toughness [57].

4 Conclusions

The present work focused on the heat treatment of the biomedical Co28Cr6Mo alloys produced by laser-based powder bed fusion (LPBF). Direct aging treatments from the as-built condition (600–900 °C for 30–180 min) were considered and effects on microstructure and hardness were assessed to identify the optimized heat treatment conditions. Once identified, preliminary assessment of wear behavior of as-built and heat-treated alloy was carried out and compared to the conventional wrought alloy. Based on the outcomes, the following conclusions can be synthetized:

- The LPBF as-built alloy is formed by a hierarchical metastable and supersaturated microstructure, characterized by the following macrostructural features: (i) solidified melt pools, (ii) epitaxial grains crossing-over the melt pools, (iii) extremely fine cellular sub-structure formed within grains. The metastable γ(Co–fcc) phase was retained in the as-built alloy.
- All aging treatments induced strengthening in the alloy. Hardness increased as a consequence of progressive transformation from γ(Co–fcc) phase into the equilibrium ε(Co–hcp) phase with increasing time and temperature (up to 850 °C).
- By increasing time and temperature, heat treatments produced a progressive modification in the LPBF as-built cellular sub-structure, that broke down into fine and homogeneously dispersed globular particles. A completely recrystallized ε(Co–hcp) microstructure was evidenced after the 850 °C for 180 min treatment.
- Dry sliding wear tests evidenced an overall good wear resistance of the as-built alloy, higher than those of conventional wrought alloy if considered conditions closer to the in-service ones (5 N). Optimized heat treatment (850 °C for 180 min) did not significantly affect wear behavior. However, a decrease in wear resistance was observed for samples with higher hardness, especially if tested at the highest normal load (10 N).

Acknowledgements This research did not receive any specific grant from funding agencies in the public, commercial, or not-for-profit sectors.

Funding Open access funding provided by Alma Mater Studiorum - Università di Bologna within the CRUI-CARE Agreement. This research did not receive any specific grant from funding agencies in the public, commercial, or not-for-profit sectors.

Declarations

Conflict of interest The authors declares that they have no conflict of interest.

References

1. Chen Q, Thouas GA (2015) Metallic implant biomaterials. Mater Sci Eng R Rep 87:1–57. https://doi.org/10.1016/j.mser.2014.10.001
2. Liverani E, Fortunato A, Leardini A et al (2016) Fabrication of Co-Cr-Mo endoprosthetic ankle devices by means of Selective Laser Melting (SLM). Mater Des 106:60–68. https://doi.org/10.1016/j.matdes.2016.05.083
3. Omar MA, Baharudin BTHT, Sulaiman S et al (2020) Characterisation of powder and microstructure, density and surface roughness for additively manufactured stent using medical grade ASTM F75 cobalt chromium (CoCrMo) by selective laser melting (SLM) technology. Adv Mater Process Technol. https://doi.org/10.1080/2374068X.2020.1860599

4. Takaichi A, Kajima Y, Kittikundecha N et al (2020) Effect of heat treatment on the anisotropic microstructural and mechanical properties of Co–Cr–Mo alloys produced by selective laser melting. J Mech Behav Biomed Mater 102:103496. https://doi.org/10.1016/j.jmbbm.2019.103496
5. Wang Z, Tang SY, Scudino S et al (2021) Additive manufacturing of a martensitic Co–Cr–Mo alloy: towards circumventing the strength–ductility trade-off. Addit Manuf 37:1–14. https://doi.org/10.1016/j.addma.2020.101725
6. Mergulhão MV, Podestá CE, das Neves MDM (2017) Valuation of mechanical properties and microstructural characterization of ASTM F75 Co-Cr alloy obtained by selective laser melting (SLM) and casting techniques. Mater Sci Forum 899:323–328. https://doi.org/10.4028/www.scientific.net/MSF.899.323
7. Qian B, Saeidi K, Kvetková L et al (2015) Defects-tolerant Co-Cr-Mo dental alloys prepared by selective laser melting. Dent Mater 31:1435–1444. https://doi.org/10.1016/j.dental.2015.09.003
8. DebRoy T, Wei HL, Zuback JS et al (2018) Additive manufacturing of metallic components – process, structure and properties. Prog Mater Sci 92:112–224. https://doi.org/10.1016/j.pmatsci.2017.10.001
9. Pillar R, Ramsay SD (2012) Cobalt-base alloys. In: Narayan RJ (ed) Mater Med Devices. ASM Interbational, pp 211–222
10. Aversa A, Lorusso M, Trevisan F et al (2017) Effect of process and post-process conditions on the mechanical properties of an A357 alloy produced via laser powder bed fusion. Metals (Basel) 7:1–9. https://doi.org/10.3390/met7020068
11. Casati R, Vedani M (2019) Aging response of an A357 Al alloy processed by selective laser melting. Adv Eng Mater 21:1800406. https://doi.org/10.1002/adem.201800406
12. Tonelli L, Liverani E, Morri A, Ceschini L (2021) Role of direct aging and solution treatment on hardness, microstructure and residual stress of the A357 (AlSi7Mg0.6) alloy produced by powder bed fusion. Metal Mater Trans B. https://doi.org/10.1007/s11663-021-02179-6
13. Kajima Y, Takaichi A, Kittikundecha N et al (2018) Effect of heat-treatment temperature on microstructures and mechanical properties of Co–Cr–Mo alloys fabricated by selective laser melting. Mater Sci Eng A 726:21–31. https://doi.org/10.1016/j.msea.2018.04.048
14. Razavi SMJ, Avanzini A, Cornacchia G et al (2021) Effect of heat treatment on fatigue behavior of as-built notched Co-Cr-Mo parts produced by Selective Laser Melting. Int J Fatigue 142:105926. https://doi.org/10.1016/j.ijfatigue.2020.105926
15. Sing SL, Huang S, Yeong WY (2020) Effect of solution heat treatment on microstructure and mechanical properties of laser powder bed fusion produced cobalt-28chromium-6molybdenum. Mater Sci Eng A 769:138511. https://doi.org/10.1016/j.msea.2019.138511
16. Song C, Zhang M, Yang Y et al (2018) Morphology and properties of CoCrMo parts fabricated by selective laser melting. Mater Sci Eng A 713:206–213. https://doi.org/10.1016/j.msea.2017.12.035
17. Béreš M, Silva CC, Sarvezuk PWC et al (2018) Mechanical and phase transformation behaviour of biomedical Co-Cr-Mo alloy fabricated by direct metal laser sintering. Mater Sci Eng A 714:36–42. https://doi.org/10.1016/j.msea.2017.12.087
18. Hussein MA, Mohammed AS, Al-Aqeeli N (2015) Wear characteristics of metallic biomaterials: a review. Materials (Basel) 8:2749–2768. https://doi.org/10.3390/ma8052749
19. Dowson D (2012) Friction and wear of medical implants and prosthetic devices. In: Narayan R (ed) Mater Med Devices. ASM International, pp 187–195
20. Merola M, Affatato S (2019) Materials for hip prostheses: a review of wear and loading considerations. Materials (Basel) 12:495. https://doi.org/10.3390/ma12030495
21. Kandahari AM, Yang X, Laroche KA et al (2016) A review of UHMWPE wear-induced osteolysis: the role for early detection of the immune response. Bone Res. https://doi.org/10.1038/boneres.2016.14
22. Kim KT, Lee S, Ko DO et al (2014) Causes of failure after total knee arthroplasty in osteoarthritis patients 55 years of age or younger. Knee Surg Relat Res 26:13–19. https://doi.org/10.5792/ksrr.2014.26.1.13
23. Chakrabarty G, Vashishtha M, Leeder D (2015) Polyethylene in knee arthroplasty: a review. J Clin Orthop Trauma 6:108–112. https://doi.org/10.1016/j.jcot.2015.01.096
24. Gang S, Fengzhou F, Chengwei K (2018) Tribological performance of bioimplants: a comprehensive review. Nami Jishu yu Jingmi Gongcheng/Nanotechnology Precis Eng 1:107–122. https://doi.org/10.13494/j.npe.20180003
25. Drummond J, Tran P, Fary C (2015) Metal-on-metal hip arthroplasty: a review of adverse reactions and patient management. J Funct Biomater 6:486–499. https://doi.org/10.3390/jfb6030486
26. Heneghan C, Langton D, Thompson M (2012) Ongoing problems with metal-on-metal hip implants. BMJ 344:10–13. https://doi.org/10.1136/bmj.e1349
27. Delaunay C, Petit I, Learmonth ID et al (2010) Metal-on-metal bearings total hip arthroplasty: the cobalt and chromium ions release concern. Orthop Traumatol Surg Res 96:894–904. https://doi.org/10.1016/j.otsr.2010.05.008
28. (2018) ASTM F75-18, Standard Specification for Cobalt-28 Chromium-6 Molybdenum Alloy Castings and Casting Alloy for Surgical Implants (UNS R30075). doi: https://doi.org/10.1520/F0075-12
29. (2020) ASTM F1537-20, Standard Specification for Wrought Cobalt-28Chromium-6Molybdenum Alloys for Surgical Implants (UNS R31537, UNS R31538, and UNS R31539). doi: https://doi.org/10.1520/F1537-20
30. Guo M, Gu D, Xi L et al (2019) Selective laser melting additive manufacturing of pure tungsten: role of volumetric energy density on densification, microstructure and mechanical properties. Int J Refract Metals Hard Mater 84:105025. https://doi.org/10.1016/j.ijrmhm.2019.105025
31. Yi JH, Kang JW, Wang TJ et al (2019) Effect of laser energy density on the microstructure, mechanical properties, and deformation of Inconel 718 samples fabricated by selective laser melting. J Alloys Compd 786:481–488. https://doi.org/10.1016/j.jallcom.2019.01.377
32. Tonelli L, Fortunato A, Ceschini L (2020) CoCr alloy processed by Selective Laser Melting (SLM): effect of Laser Energy Density on microstructure, surface morphology, and hardness. J Manuf Process 52:106–119. https://doi.org/10.1016/j.jmapro.2020.01.052
33. Taylor RNJ, Waterhouse RB (1983) A study of the ageing behaviour of a cobalt based implant alloy. J Mater Sci 18:3265–3280. https://doi.org/10.1007/BF00544151
34. Klarstrom D, Crook P, Wu J (2004) Metallography and Microstructures of Cobalt and Cobalt Alloys. In: Vander Voort GF (ed) Metallogr Microstruct ASM Handb, vol 9. ASM International, pp 762–774
35. (2017) ASTM G77 -17, Standard Test Method for Ranking Resistance of Materials to Sliding Wear Using Block-on-Ring Wear Test. doi: https://doi.org/10.1520/G0077-17
36. Williams JA, Dwyer-Joyce RS (2001) Contact between solid surfaces. In: Bhushian B (ed) Modern Tribology Handbook. CRC Press, pp 121–162
37. Bhadeshia HKDH (2012) Steels for bearings. Prog Mater Sci 57:268–435. https://doi.org/10.1016/j.pmatsci.2011.06.002
38. Papadakis EP, Stickels CA, Innes RC (1995) An ultrasonic technique for measuring the elastic constants of small samples. SAE Tech Pap 104:830–837. https://doi.org/10.4271/950897

39. Mergulhão MV, Podestá CE, das Neves MDM (2018) Perspective of Additive Manufacturing Selective Laser Melting in Co-Cr-Mo Alloy in the Consolidation of Dental Prosthesis. In: Dobrzański LA (ed) Biomaterials in Regenerative Medicine. IntechOpen, Rijeka, Ch. 6
40. Rao JH, Zhang Y, Zhang K et al (2019) Multiple precipitation pathways in an Al-7Si-0.6Mg alloy fabricated by selective laser melting. Scr Mater 160:66–69. https://doi.org/10.1016/j.scriptamat.2018.09.045
41. Molinari A (2017) The structural metastability of metallic alloys produced by Selective Laser Melting. La Metall Ital 1:21–27
42. Takaichi A, Suyalatu NT et al (2013) Microstructures and mechanical properties of Co-29Cr-6Mo alloy fabricated by selective laser melting process for dental applications. J Mech Behav Biomed Mater 21:67–76. https://doi.org/10.1016/j.jmbbm.2013.01.021
43. Prashanth KG, Eckert J (2017) Formation of metastable cellular microstructures in selective laser melted alloys. J Alloys Compd 707:27–34. https://doi.org/10.1016/j.jallcom.2016.12.209
44. Seyedi M, Zanotto F, Monticelli C et al (2018) Microstructural characterization and corrosion behaviour of SLM CoCrMo alloy in simulated body fluid. Metall Ital 110:45–50
45. Liverani E, Balbo A, Monticelli C et al (2017) Corrosion resistance and mechanical characterization of ankle prostheses fabricated via selective laser melting. Procedia CIRP 65:25–31. https://doi.org/10.1016/j.procir.2017.04.037
46. Li H, Wang M, Lou D et al (2020) Microstructural features of biomedical cobalt–chromium–molybdenum (CoCrMo) alloy from powder bed fusion to aging heat treatment. J Mater Sci Technol 45:146–156. https://doi.org/10.1016/j.jmst.2019.11.031
47. D'Lima DD, Steklov N, Fregly BJ et al (2008) In vivo contact stresses during activities of daily living after knee arthroplasty. J Orthop Res 26:1549–1555. https://doi.org/10.1002/jor.20670
48. Sharma A, Komistek RD, Ranawat CS et al (2007) In vivo contact pressures in total knee arthroplasty. J Arthroplasty 22:404–416. https://doi.org/10.1016/j.arth.2006.07.008
49. Glascott J, Stott FH, Wood GC (1985) The effectiveness of oxides in reducing sliding wear of alloys. Oxid Met 24:99–114. https://doi.org/10.1007/BF00664227
50. Wilson JE, Stoot FH, Wood GC (1980) The development of wear-protective oxides and their influence on sliding friction. Proc Roy Soc A 369:557–574
51. De Faria DLA, Venâncio Silva S, De Oliveira MT (1997) Raman microspectroscopy of some iron oxides and oxyhydroxides. J Raman Spectrosc 28:873–878. https://doi.org/10.1002/(sici)1097-4555(199711)28:11%3c873::aid-jrs177%3e3.0.co;2-b
52. Oh SJ, Cook DC, Townsend HE (1998) Characterization of iron oxides commonly formed as corrosion products on steel. Hyperfine Interact 112:59–66. https://doi.org/10.1023/a:1011076308501
53. Hanesch M (2009) Raman spectroscopy of iron oxides and (oxy) hydroxides at low laser power and possible applications in environmental magnetic studies. Geophys J Int 177:941–948. https://doi.org/10.1111/j.1365-246X.2009.04122.x
54. Blau PJ (2017) Sliding and adhesive wear. In: Totten GE (ed) Frict Lubr Wear Technol ASM Handb, vol 18. ASM International, pp 313–322
55. Hornbogen E (1975) The role of fracture toughness in the wear of metals. Wear 33:251–259. https://doi.org/10.1016/0043-1648(75)90280-X
56. Hutchings I, Shipway P (2017) Wear by hard particles. In: Tribol. - Frict. Wear Eng. Mater., 2nd edn. Butterworth-Heinemann, pp 165–233
57. De Mol Van Otterloo JL, De Hosson JTM (1997) Microstructure and abrasive wear of cobalt-based laser coatings. Scr Mater 36:239–245. https://doi.org/10.1016/S1359-6462(96)00346-6